Iranian Journal of Physics Research, Vol. 25, No. 3, 2025
DOI: 10.47176/ijpr.25.1.22025

# Silver-doped ZnO nanorods (Ag-ZNRs): preparation and characterization

**Sarah Kamel Khadem and Araa Mebdir Holi,***
Department of Physics, College of Education, University of Al-Qadisiyah, Al-Diwaniyah, Al-Qadisiyah 58002, Iraq

E-mail: araa.holi@qu.edu.iq

(Received 18 December 2024; in final form 16 April 2025)

**Abstract**
In this study, ZnO nanorods (ZNRs) were synthesized via the hydrothermal method and doped with silver (Ag). The structural, morphological, and optical properties of pure and Ag-doped ZNRs were characterized using X-ray diffraction (XRD), UV-visible spectroscopy (UV-Vis), energy-dispersive X-ray (EDX) analysis, field emission scanning electron microscopy (FE-SEM), and photoluminescence (PL) spectroscopy. XRD confirmed the hexagonal wurtzite structure of the Ag-doped ZNRs, while FE-SEM revealed high-aspect-ratio nanorod morphology. UV-Vis analysis showed a reduction in the direct band gap with increasing Ag doping concentration. PL spectra exhibited enhanced emission intensity upon Ag doping, suggesting modified recombination dynamics, potentially due to suppressed non-radiative pathways or increased radiative transitions. These findings indicate that Ag-doped ZNRs hold promise for optoelectronic applications, including light-emitting devices.

**Keywords:** Zinc Oxide Nanorods (ZNRs); Ag-doped ZNRs; Hydrothermal method.

## 1. Introduction

Zinc oxide, or ZnO, is an inorganic binary compound material with dual piezoelectric and semiconducting properties that belongs to the II-VI material groups. ZnO is transparent to visible light and has a large direct band gap of 3.37 eV at ambient temperature [1]. The exciton binding energy in ZnO is about 60 meV [2]. This high binding energy contributes to the stability of excitons at room temperature, facilitating applications in lasers and photonic devices [3]. For solar energy harvesting devices that produce photo-electrons for photovoltaic, photodetective, and photocatalysis systems, ZnO nanostructures are highly helpful in special ZnO nanorods (ZNRs.) Moreover, ZNRs can be utilized in chemical pesticides [4], bactericides, and photocatalysts [5] due to their properties.

ZNRs are used in blue light-emitting diodes and short-wavelength lasers. Also, nanostructured transition metals doped with ZnO are promising magnetic semiconductor materials for spintronic [6]. To obtain the desired properties, metal oxides can be combined with noble metals like silver. Because it is non- toxic and has superior electrical and thermal conductivity when compared to other noble metals, it is widely employed [7].

By altering the oxygen vacancies and crystal defects, doping Ag ions into ZnO produces additional changes in the absorbance, physical, and chemical properties that contribute to increasing the material's photocatalytic activity [8]. By creating a Schottky barrier using ZnO, it suppresses the rate of recombination. In addition, it creates intermediate energy states that lower the band gap and require less energy to excite electrons [9, 10]. ZnO's silver can trap the charge carrier and block the charge recombination process [11]. Ag-doped ZnO exhibits ferromagnetic [12] and antibacterial [13] characteristics. A silver band forms and interacts with ZnO's d orbital, causing the ferromagnetic characteristics. ZnO's band gap is modified and its band structure is altered by adding Ag, which makes ZnO appropriate for solar cells [14]. Several approaches, including the acid-catalyzed sol-gel technique [15], thermal treatment [16], sonochemical [17], and co- precipitation [18], were employed by various researchers in the development of the Ag-doped ZNRs.

This paper presents an experimental hydrothermal method that focuses on the synthesis and characterization of Ag-doped ZNRs. When doping and hydrothermal techniques are properly combined, it is feasible to produce NRs with improved characteristics over undoped ZnO. This effort involved a complementary investigation of Ag-doped ZNRs using X-ray diffraction (XRD), photoluminescence (PL), field emission scanning electron microscopy (FE-SEM), and UV-visible spectroscopy (UV-Vis). This project's objective was to create Ag-doped ZNRs and change their characteristics such that they may be utilized in optoelectronic devices. In particular, the study discusses how Ag concentration affects ZNR film structural, morphological, optical, and PL characteristics.

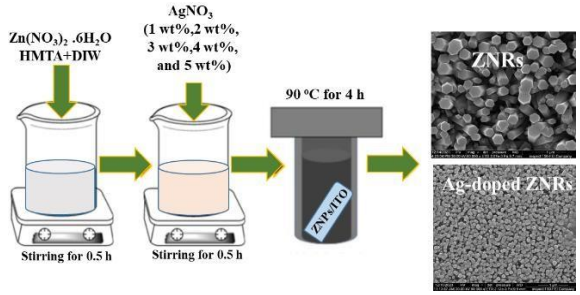


**Figure 1.** Schematic diagram of hydrothermal method of Ag-doped ZNR s.

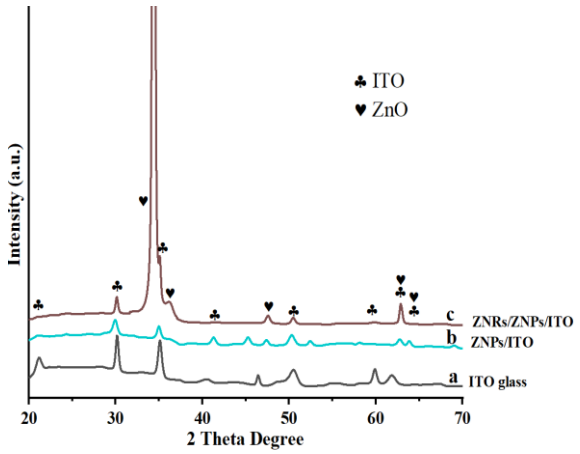


**Figure 2.** XRD patterns (a) ITO glass, (b) ZNPs/ITO, and (c) ZNRs/ ZNPs/ITO.

This information is crucial in determining the films' suitability for optoelectronic applications.

## 2. Experimental

### 2.1. Synthesis of ZNRs and Ag-doped ZNRs

Synthesis of ZNRs and Ag-doped ZNRs includes 5 steps: The first step involves pretreatment of the substrates. Initially, the substrates consisted of glass sheets with a thin conductive layer of saturated indium tin oxide ($SnO_2$: In, ITO). ITO is one of the most widely used transparent conducting oxide (TCO). The resistance of the sheet is about (20 Ω/cm$^2$) for one side consuming dimensions of {(3x1) cm$^2$}. Subsequently, ITO glass substrates were treated by immersing them in an acetone beaker for fifteen minutes to do an ultrasonic bath (Ultrasonic LC 30 H ELMA). Following that, the sonication procedure was carried out again in isopropanol alcohol, 100% ethanol, and deionized water (DIW) independently in order to eliminate the first oxide coatings from the substrates' surfaces. The substrates were rinsed with DI water during the sonication procedure. The seeds were deposited employing a spin coating technique on an ITO glass substrate. 0.2 mol/L zinc acetate 2 hydrate [Zn $(CH_3COO)_2.2H_2O$] and 0.2 mol/L diethanolamine $NH(CH_2CH_2OH)_2$ have been mixed to create the gel solution for coating. The ethanolic mixture was then stirred for 30 minutes at 60 °C, to produce a colloidal, homogenous solution that was suspended for the entire night.

Table 1: XRD analysis for ZNPs and ZNRs

| Structural | St. Value | Z NPs/ITO | | | ZNRs/ZNPs/ITO | | |
|---|---|---|---|---|---|---|---|
| ***hkl*** | (200) | (100) | (002) | (101) | (100) | (002) | (101) |
| 2Θ$^o$ | 34.467 | - | 34.9636 | - | 30.1081 | 34.3524 | 36.1791 |
| d- (nm) | 2.600 | - | 2.56634 | - | 2.96821 | 2.61059 | 2.48081 |
| FWHM | - | - | 0.49593 | - | 0.33062 | 0.26863 | 0.91245 |

Subsequently, spin deposition was carried out by spinning the ITO glass substrates for 30 seconds at 3500 rpm using 100 µL of the prepared solution for each sample. Ultimately, ZnO nanoparticles (ZNPs) were formed on ITO glass by annealing the samples for two hours at 350 °C.

The fourth step (figure 1) involves making the detailed calculation of the doping percentage of silver has been done using the required amount of silver nitrate (1%, 2%, 3%, 4%, and 5%) was added into an aqueous solution containing the [$Zn(NO_3)_2.6H_2O$ + Hexamethylenetetramine (HMTA)] then stirred for about 30 minutes at room temperature. Next, the seed layer samples were immersed in this prepared solution for 4 hours at 90 °C. Subsequently, the Ag-doped ZNR samples are released to air dry.

### 2.2 Characterization

The samples' phases and structure were examined using X-ray diffraction (a Shimadzu 6000 diffractometer) utilizing Cu-Kα radiation at 40 kV and 30 mA (λ=1.4506 Å). The produced samples' absorbance spectra were measured by utilizing a ( Shimadzu UV-1800) ultraviolet-visible spectrophotometer. The morphologies of all samples were studied via a field emission scanning electron microscope FE-SEM (Nova Nano SEM 450) coupled to energy-dispersive X-ray spectroscopy (EDS). Photoluminescence (PL) spectra were recorded from 350 to 800 nm at room temperature by a 325 nm excitation (Shimadzu RF-5301PC spectrometer, Japan).

## 3. Results and Discussion

Every sample that was studied had a hexagonal wurtzite structure, both the pure ZNRs and the ZNRs doped with silver. All samples have high crystallinity, as shown by the strong diffraction peaks in figures 2 and 3. The diffraction angle, d-spacing, and full width at half maximum (FWHM) of ZNPs and ZNRs are presented in Table 1. Figure 2 displays the XRD patterns of ITO glass, ZNPs/ITO/glass, and ZNRs/ZNPs/ITO/glass, based on the two JCPDS cards (no. 01-089-4598) & (no. 00-003-0888) for ITO glass substrate and ZNRs, respectively.

Ag-doped ZNRs XRD pattern shows a slight shift in the direction of the 34° angles at the position of the (002) peaks [19], as figure 3 illustrates. As silver doping increases, peak broadening is accompanied by a decrease in diffraction peak strength. The crystalline quality of the generated nanoparticles declines with increasing silver doping. At the locations where the positively orientated (002) crystal plane has shifted, silver ions must replace zinc ions. The shift in (002) peaks may be due to the difference in ionic radii of zinc and silver, rather than the weight proportion of doped silver because the ionic radius of silver ions is higher than that of zinc ions [20].

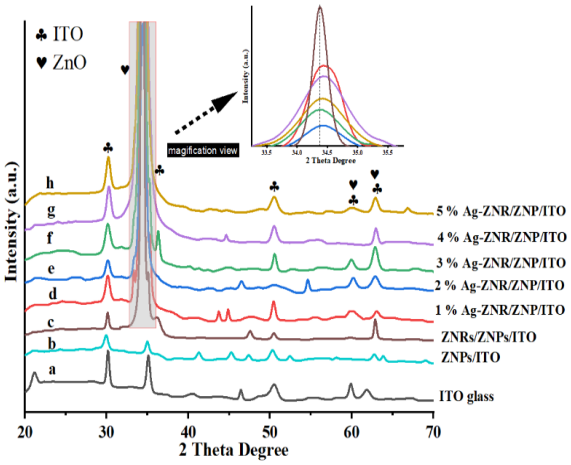


**Figure 3.** XRD diffractograms of (a) ITO glass; (b) ZNPs/ITO; (c) pure ZNRs/ZNPs/ITO; and ZNRs doped with different concentrations of Ag: (d) 1%; (e) 2%; (f) 3%; (g) 4%; and (h) 5%.

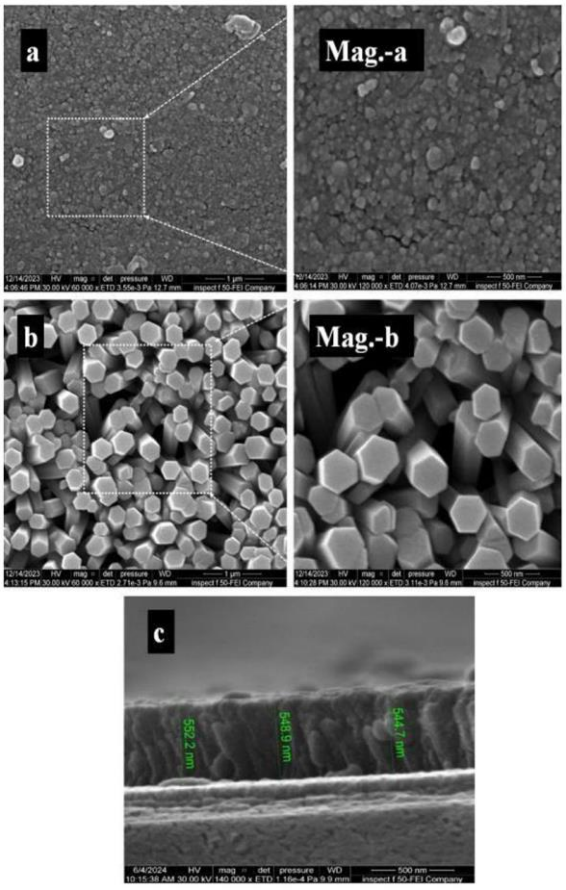


**Figure 4.** Field emission scanning electron microscopic images of the (a) ZNPs and (b) ZNRs at different scales and Magnifications; (c) cross-section of pure ZNRs

The comparison of diffraction patterns between ZNRs and Ag doped-ZNRs reveals that the diffraction peaks of pure ZNRs, particularly at around 34°, exhibit a mixture with the silver signal, indicating successful integration of Ag into the ZnO crystal lattice due to the smaller ionic radius of $Zn^{2}$ (74 pm) compared to $Ag^{1}$ (126 pm) [21]. This integration results in the acquisition of a metallic silver phase on the ZnO surface.

Table 2. XRD analysis for ZNRs and Ag- ZNRs grown on ITO glass substrates at different Ag concentrations

| Ag | 2Θ°-(002) | FWHM (Å) | dhkl exp. (Å) | Crystalline size (nm) | dhkl Std. (Å) | Lattice strain % | (*hkl*) |
|---|---|---|---|---|---|---|---|
| 0% | 34.35241 | 0.26863 | 2.61059 | 32.32 | 2.600 | 0.378731357 | (002) |
| 1% | 34.3190 | 0.48806 | 2.61305 | 17.79 | 2.600 | 0.688097479 | (002) |
| 2% | 34.3982 | 0.79310 | 2.60721 | 10.95 | 2.600 | 1.118161929 | (002) |
| 3% | 34.3959 | 0.85411 | 2.61055 | 9.700 | 2.600 | 1.204177638 | (002) |
| 4% | 34.4154 | 0.91512 | 2.60596 | 9.500 | 2.600 | 1.290193348 | (002) |
| 5% | 34.3931 | 0.91512 | 2. 6076 | 9.600 | 2.600 | 1.290193348 | (002) |

Table 3. The estimation of lattice parameters for ZNRs and Ag-ZNRs grown on ITO glass substrates at different Ag concentrations.

| Ag | 2Θ°-[002] | c (Å) | Lattice strain % in the z-axis | 2Θ°-[100] | a (Å) | Lattice strain % in a-axis | c/a |
|---|---|---|---|---|---|---|---|
| 0% | 34.35 | 5.2168 | 0.2049 | 30.20 | 3.3325 | 3.3325 | 1.565 |
| 1% | 34.31 | 5.2217 | 0.2995 | 30.30 | 3.3213 | 3.3213 | 1.572 |
| 2% | 34.39 | 5.2101 | 0.0755 | 30.39 | 3.3113 | 3.3113 | 1.573 |
| 3% | 34.39 | 5.2105 | 0.0837 | 30.39 | 3.3113 | 3.3113 | 1.573 |
| 4% | 34.41 | 5.2076 | 0.0270 | 30.46 | 3.3048 | 3.3048 | 1.575 |
| 5% | 34.39 | 5.2108 | 0.0899 | 30.33 | 3.2825 | 3.2825 | 1.587 |

Moreover, an increase in Ag concentration leads to a broadening of the diffraction peaks as shown in Table 2, suggesting a correlation between Ag content and peak broadening [21]. This broadening phenomenon could be attributed to the structural changes induced by the higher concentration of Ag dopants in the ZnO nanorods, influencing their crystalline properties and diffraction patterns.

Moreover, as the concentration of Ag dopant increases, the FWHM also increases, indicating a change in the crystallinity of the ZnO nanorods. This change in FWHM suggests that higher Ag concentrations may promote the preferred growth of nanorods along the c-axis, influencing the structural properties of the synthesized materials [22]. The addition of Ag ions to ZnO nanorods causes expansion in lattice constants (tensile strain) due to the larger atomic radius of Ag compared to Zn, leading to changes in lattice parameters [23]. The particle size of the ZNRs and Ag-ZNRs has been calculated by using Debye–Scherrer's formula [24].

The lattice parameters for ZNRs and Ag-ZNRs synthesized at various concentrations of Ag show hexagonal unit cells that are extremely similar to the typical lattice parameter values for ZnO (**a** = 3.2998 Å and **c** = 5.2066 Å). The peaks from the wurtzite phase were used to derive the lattice constants. From the peaks with orientation (100), constant **a** was estimated, and constant **c**-for orientation (002) was presented. Table 3 presents the lattice parameters. Remarkably, compared to low concentrations, the c/a ratio is higher at high Ag concentrations, which may be attributed to a significantly greater lattice mismatch.

Figure 4(a) presents the FE-SEM image of ZNPs (seed layer) with 3 layers. As observed the prepared ZNPs were very compact and did not have any cracks as observed from their morphology figure 4(b) shows FE- SEM images of ZNRs grown for 4 hr, with an average length of

around ~500 nm, indicating that rods are emerging on the nucleation sites ZNPs.

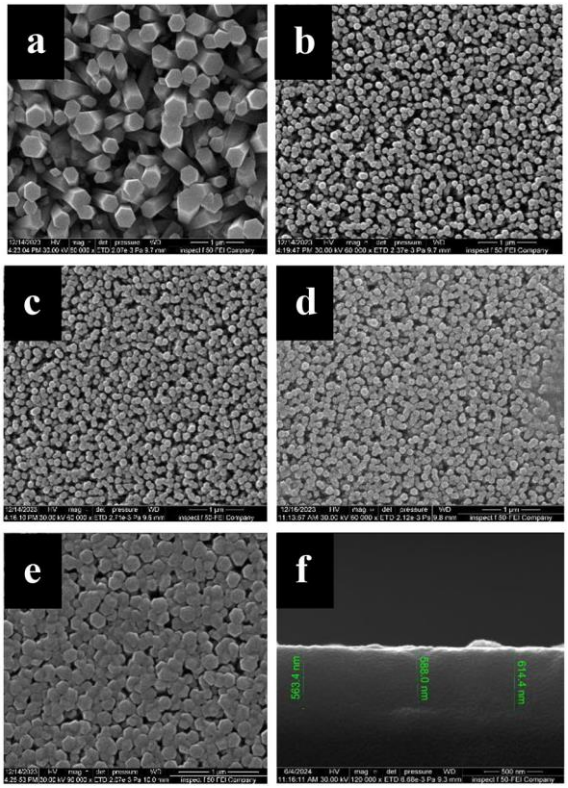


**Figure 5.** Field emission scanning electron microscopic images of the ZNRs doped with different concentrations of Ag: (a) 1%; (b) 2%; (c) 3%; (d) 4%; and (e) 5 %; (f) cross-section of 4 % Ag- doped ZNRs.

A FE-SEM image with (0, 1, 2, 3, 4, and 5) weight percentage Ag- doped ZNRs is shown in figure 5. Non-uniformity in the size of particles and particle aggregation are seen in the FE-SEM micrographs. Agglomeration increases as Ag doping concentration rises, possibly due to Ag nanoparticle formation [25, 26]. Every FE-SEM image demonstrates the reduction in the diameter of rods. ZnO nanoparticles have a spherical aggregation of doped particles and a cylindrical rod-like shape, with an average length of around ~600 nm, agglomeration happens practically everywhere in the crystallite form.

The dispersive X-ray (EDX) spectra of 1%, 2%, and 3% of Ag are displayed in figures 6 (a, b, and c). They only comprise Zn and O elements along with other elements from the ITO/glass substrate due to the small amount of Ag metal. Whilst the 4% and 5% Ag-doped ZNRs samples, figure 6(d and e), have notable doping concentrations of Ag elements, which also contain O and Zn elements.

The UV-Vis absorbance spectra, ranging from 300 to1000 nm, of two different samples, the ZNRs and various Ag-doped ZNRs, are displayed in figure 7. An absorption edge develops at approximately 383 nm, which could be a sign of ZnO NRs' inherent band gap transition. In contrast to pure ZNRs, various Ag-doped ZNRs will have a significantly larger optical absorption edge. Furthermore, figure 8 clearly showed an elevated absorption in the visible light region when Ag was added to ZNRs. This demonstrates that adding Ag to ZnO reduces the band gap. The energy gap values are displayed in Table 4.

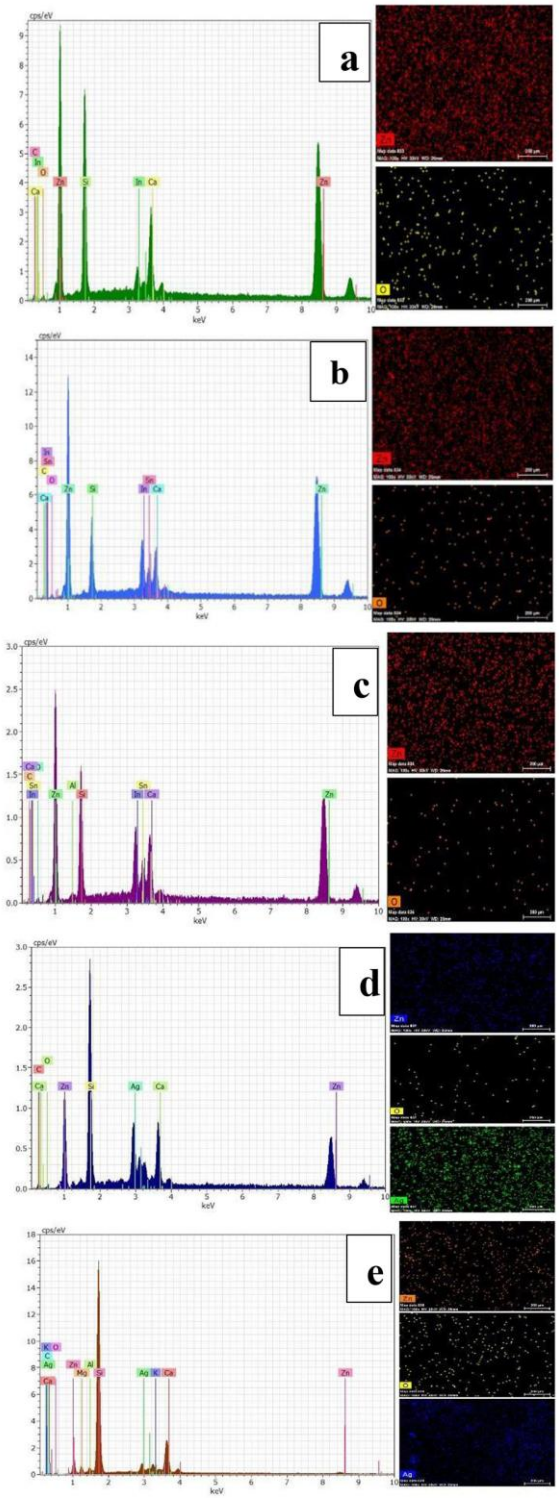


**Figure 6.** EDS patterns of ZNRs doped with different concentrations of Ag: (a) 1%; (b) 2%; (c) 3%; (d) 4%; and (e) 5%.

With an increase in doping concentration, the band gap value decreases, as indicated by the shift in the absorption edge. Numerous variables, like lattice strain, carrier concentration, grain size, etc., affect how the *Eg* value changes [27]. The formation of energy levels in the

valence and conduction bands is responsible for the band gap's decreasing.

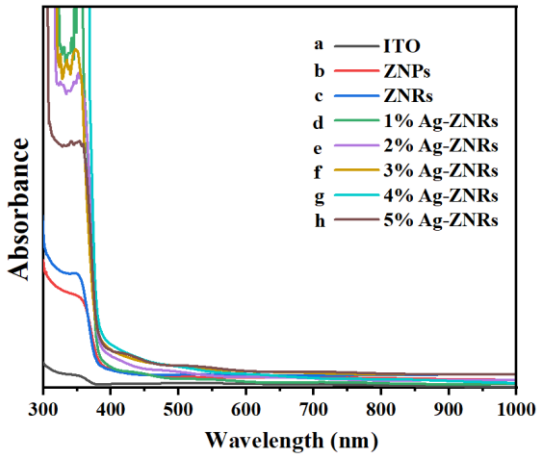


**Figure 7.** UV–Vis spectra curves of (a) ITO glass; (b) ZNPs/ITO; (c) pure ZNRs/ZNPs/ITO; and ZNRs doped with different concentrations of Ag: (d) 1%; (e) 2%; (f) 3%; (g) 4%; and (h) 5 %.

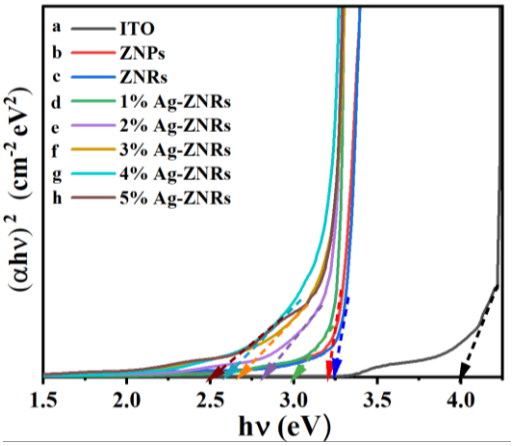


**Figure 8.** Band gap energy curves of (a) ITO glass; (b)ZNPs/ITO; (c) pure ZNRs/ZNPs/ITO; and ZNRs doped with different concentrations of Ag: (d) 1%; (e) 2%; (f) 3%; (g) 4%; and (h) 5 %.

Ag-doped ZNRs may be taken into consideration to enhance the optical characteristics. In actuality, ZNRs' optical absorption can be improved by a tiny quantity of Ag. The introduction of Ag into the ZnO structure alters its properties, leading to a decrease in the bandgap and a shift towards a more conductive behavior, as indicated by the decrease in resistivity with Ag doping. The interaction between Ag and ZnO influences the optical properties of the films, making them promising materials for applications such as photovoltaics due to their improved performance [28]. Ag doping has reduced the energy gap of ZnO; this means that the modification in the allowed band edge leads to a downward shift in the conduction band edge accompanied by shrinkage of the optical band gap due to Ag incorporation in the ZnO NRs lattice. Substitutional $Ag^{+}$ ions (ionic radius ~1.26 Å) can replace $Zn^{2+}$ (0.74 Å) in the ZnO lattice [29]. This causes lattice distortion and local electric field modification, leading to conduction band edge downshift and hence reduced bandgap. Possibly increased density of states near the conduction band.

Table 4: The energy gap values of pure ITO, ZnO NPs, ZnO NRs, and different concentration Ag-doped ZNRs.

| Constructions | Energy gap (eV) |
|---|---|
| ITO/glass | 4.0 |
| ZNPs/ITO/glass | 3.22 |
| ZNRs/ ZNPs /ITO/glass | 3.20 |
| 1% Ag-doped ZNRs | 3.00 |
| 2% Ag-doped ZNRs | 2.82 |
| 3% Ag-doped ZNRs | 2.67 |
| 4% Ag- doped ZNRs | 2.61 |
| 5% Ag-doped ZNRs | 2.50 |

Photoluminescence (PL) describes the phenomenon of light emission from any form of matter after the absorption of photons (electromagnetic radiation) [30]. The room temperature photoluminescence (PL) spectra of various concentrations of Ag-doped ZNRs and pure ZNRs, as shown in figure 9, were recorded using a Xenon lamp that had a wavelength of excitation of 325 nm for the wavelength range of 200- 800 nm. The photoluminescence spectra of ZNRs indeed show an increase in emission intensity with higher Ag-doping concentrations, as observed in the research by Abdalla et al. [31]. This enhancement in emission intensity can be attributed to the presence of oxygen vacancies in the Ag-doped films, as suggested by Ahmed et al. [18].

Both inherent and extrinsic flaws in ZnO are the cause of this visible emission, figure 9. For the pure ZNRs sample and Ag-doped ZNRs as observed from figure 9, the PL spectra show four emission bands with varying intensities at wavelengths of 325, 360, 650, and 700 nm. The optical excitation is responsible for the peak at 325 nm, whereas the presence of zinc interstitial defect in the ZnO lattice is responsible for the peak at 360 nm. The radiating flaws and the interface traps clinging to the grain boundaries may be the cause of the green emission peaks at 650 nm. Deep-level emission (DLE), a term used to describe visible emission, may be associated with variations in inherent defects in zinc oxide, including interstitial zinc, interstitial oxygen, zinc vacancy, and oxygen vacancy [32]. The emission results from photo-initiated hole recombination with a single-ionized charge state of the point defects (Zn interstitial and oxygen vacancies) and electron recombination in single-ionized oxygen vacancies [33]. Several parameters, including particle size, structural defects, and oxygen vacancies, were reported to have an impact on the PL spectra of nanostructures in the literature [34]. The increase in the insanity of PL spectra toward a high wavelength known as the red region is observed with increasing silver concentration. The rising concentration of oxygen vacancies on surface ZNRs could be the cause of the redshift [35]. Peak intensity at 700 nm is attributed to oxygen vacancies and is observed to increase at 1%, and then, it decreases as Ag doping concentration in the ZNRs increases from 2% to 3 % [36, 37]. When Ag doping concentration arrived at 4%, the intensity at (700) nm, first rose before falling again at a concentration of 5 %. This can be explained by two distinct methods for the incorporation of $Ag^{+}$ ions into the ZnO nanostructures:

the replacement of $Zn^{+}$ ions, which creates additional ionized oxygen vacancies, and the inclusion of Ag as interstitials.

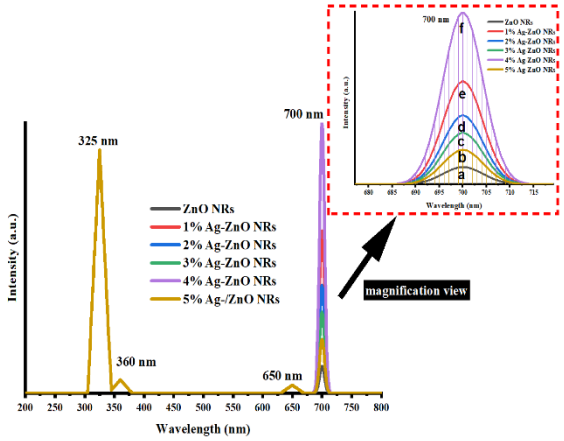


**Figure 9.** Photoluminescence spectra of: (a) pure ZNRs; and ZNRs doped with different concentrations of Ag: (b) 1%; (c) 2%; (d) 3%; (e) 4%; and (f) 5 %.

On the other hand, the majority of the "Ag" ions may have been substituted into the lattice of ZnO at low Ag doping concentrations. More Ag ions (5 %) are interstitially incorporated into the ZnO nanostructure at higher Ag doping concentrations. Therefore, more lattice defects are produced in ZnO nanostructures with greater Ag doping concentrations [38].

The increase in PL intensity (4 %) suggests a decrease in defects and surface passivation due to localized surface plasmon resonance coupling between the doped silver and ZNRs. Overall, silver doping enhances the recombination processes, making these materials more efficient for optoelectronic devices. However, excessive silver doping (5%) can lead to quenching of photoluminescence due to spectral self-absorption of the silver nanoparticle surface plasmon resonance. As mentioned in earlier studies [39-42], the 700 nm emission band of undoped ZNRs was demonstrated to be connected to an excess of oxygen vacancies. In this approach, Ag doping transforms ZnO from a UV emitter to a broadband emitter or even a red/NIR emitter. Thus, it is suitable for different optoelectronic devices because Ag doping enhances and broadens emission. While traditional ZnO applications focus on UV, Ag-doped ZNRs push the material into new roles in optoelectronics [43]. It is noteworthy that the PL intensity of Ag- doped ZNRs is significantly higher than that of undoped ZNRs. The red-light region's greatest emission can be found at 700 nm. Ag-doped ZNRs have a higher intensity of free exciton emission at 700 nm in comparison to undoped ZNRs. Increased emission intensity following Ag doping is shown in figure 9, indicating changes in electron-hole recombination dynamics. This implies that Ag doping improves ZNRs' optical characteristics by either boosting radiative transitions or blocking non-radiative routes. This enhancement is most likely due to blocking non-radiative recombination paths, which may explain the trap passivation brought on by Ag dopants. Furthermore, the Ag atoms offer shallow-level energy states that promote the radiative transition, and the effective radiative recombination can be improved [44]. It is observed in figure 9 that no significant redshift is observed, despite the expected increase in strain due to the larger ionic radius of $Ag^{+}$ compared to $Zn^{2+}$ [45]. This absence suggests that the quantum confined Stark effect (QCSE) may be either too weak to be spectrally resolved or overshadowed by competing optical processes. In that Ag, doping introduces localized states within the bandgap and contributes to bandgap narrowing, which significantly alters the recombination dynamics. These new pathways often lead to enhanced defect-level emissions in the visible to near-IR range, potentially masking QCSE-induced shifts. As a result, no significant redshift or broadening is observed in the PL emission, suggesting a reduced influence of spontaneous polarization on the optical response [46].

The three steps below are involved in the UV emission process of the PL from ZNRs, as per the mechanism of exciton emission: pure ZNRs sample is excited by incident light, which also creates carriers. The carriers subsequently relax to the conduction band edge and form excitons through phonon scattering. The excitons then propagate within the crystal, and their recombination releases photons. Ag atoms occupy Zn atom positions in the ZNR lattice for Ag-doped ZnO films. The carriers in the sample would be excited by the incident UV radiation. Excitons quickly diffuse in ZnO due to the photo-carriers' easier escape from Ag ions than from Zn ions, increasing to electron-hole pairs (excitons). A higher concentration of excitons will also result in a higher possibility of excitonic recombination. As a result, Ag-doped ZnO emits red light with a greater intensity than undoped ZnO. Because of the strong link between ZNRs and silver particles, the photoluminescence intensity of Ag-doped ZNRSs is higher than that of ZNRs without Ag. This indicates that the metal-semiconductor composite is well-orientated for laser diode material use; Lu et al. [47] showed this phenomenon well-marked. Based on these results, Ag doping is a key factor in changing the optical properties of ZNRs, which makes it a viable option for a range of optoelectronic uses such as light-emitting diodes (LEDs).

## Conclusion

A straightforward hydrothermal process was utilized to effectively synthesize both pure ZNRs and Ag-doped ZNRs. XRD confirmed that hexagonal wartzite and polycrystalline structures are present in all of the prepared films. FE-SEM images demonstrated the reduction in the diameter of rods after doping. Ag doping leads to a decrease in band edge absorption while enhancing visible emission. This indicates a modification in the recombination dynamics of electron-hole pairs, essential for LED functionality. When silver (Ag) is added to ZNRs, it is discovered that the PL intensity is higher than in pristine (undoped) ZNRs. In general, silver ions are essential for passivating surface defect states and extending ZNRs' PL intensity. Understanding the impact of silver doping provides important insights for developing robust and efficient optoelectronic devices using ZNRs.

## References


1. V N Hegde, J. Sci. Adv. Mater. Devices **9** (2024) 100733.
2. S Arora , S Dhar, Appl. Phys. Lett. **122** (2023) 20.
3. B Gharbi, A Taabouche, M Brella, F Chelgham, , A Mamanou, J. Electr. Syst. **20** (2024) 995.
4. K Duraisamy, M Amirthalingam, T Govindhan, J C Kim, K Hasegawa, S Palanisamy, Mater. Lett. **317** (2022) 132098.
5. K Kairyte, A Kadys, Z Luksiene, J. Photochem. Photobiol. B **128** (2013) 78.
6. D Anbuselvan et al., Physica E **129** (2021) 114665.
7. A Dhaka, S C Mali, S Sharma, R Trivedi, Results Chem. **2023** (2023) 101108.
8. A HernJndez-Ramxrez, I. Medina-Ramxrez, Photocatalytic Semiconductors, Springer, Cham (2015).
9. Y Sun, W Zhang, Q Li, H Liu, X Wang, Adv. Sens. Energy Mater. **2023** (2023) 100069.
10. L J Brillson, Y Lu, J. Appl. Phys. **109** (2011).
11. B Abebe, G Amenu, D T Leku, Surf. Interfaces **39** (2023) 102946.
12. Y Liu, H Qingyu, S Shulin, X Zhenchao, Vacuum **173** (2020) 109127.
13. K B Ranjith et al., Physica E **133** (2021) 114801.
14. L Li, T Zhai, Y Bando, D Golberg, Nano Energy **1** (2012) 91.
15. C Thangaraju, A J Lenus, N V Jaya, Mater. Res. Express **7** (2020) 015011.
16. H A Thabit et al., Nanomaterials **12** (2022) 3068.
17. C Karunakaran, V Rajeswari, P Gomathisankar, J. Alloys Compd. **508** (2010) 587.
18. D S Ahmed, M R Mohammed, M K Mohammed, Nanosci. Nanotechnol. Asia **10** (2020) 127.
19. R Raji, K S Sibi, K G Gopchandran, Appl. Surf. Sci. **427** (2018) 863.
20. J Fan, R Freer, J. Appl. Phys. **77** (1995) 4795.
21. Gohar, Authorea Preprints (2024).
22. T T H Pham et al., RSC Adv. **12** (2022) 7850.
23. A Seidu, E Martin, G Gebreyesus, G Nkrumah-Buandoh, MRS Adv. **3** (2018) 2643.
24. A O Bokuniaeva, A S Vorokh, J. Phys.: Conf. Ser. **1410** (2019) 012057.
25. R Singh, P B Barman, D Sharma, J. Mater. Sci. Mater. Electron. **28** (2017) 5705.
26. A M Oda et al., Int. J. Chem. **7** (2015) 39.
27. R Krithiga, G Chandrasekaran, J. Cryst. Growth **311** (2009) 4610.
28. M M Abouelela et al., Mater. Chem. Phys. **305** (2023) 127984.
29. E S Nour et al., AIP Adv. **5** (2015).
30. K N Shinde et al., Phosphate Phosphors for Solid-State Lighting (2012) 41.
31. A M Abdalla et al., Radiat. Phys. Chem. **210** (2023) 110999.
32. A S Razeen, A-S Gadallah, M M El-Nahass, Physica B **538** (2018) 131.
33. Y Yang et al., Solid State Commun. **138** (2006) 521.
34. Y Gong et al., Nanoscale Res. Lett. **2** (2007) 297.
35. J Lv, M Fang, Mater. Lett. **218** (2018) 18.
36. Z N Kayani et al., Opt. Quant. Electron. **52** (2020) 1.
37. Lupan et al., Sens. Actuators B **223** (2016) 893.
38. R S Zeferino, M. Barboza Flores, U. Pal, J. Appl. Phys. **109** (2011).
39. A S Kuznetsov et al., Opt. Mater. Express **2** (2012) 723.
40. C Klingshirn, Phys. Status Solidi B **244** (2007) 3027.
41. G Chai et al., J. Phys. Chem. C **115** (2011) 2907.
42. V V Osiko, Optika i Spektroskopiya **6** (1959) 770.
43. S Chandran et al., J. Mol. Struct. **1311** (2024) 138310.
44. M M. Abouelela et al., Electrochem. Commun. **158** (2024) 107645.
45. S Sagadevan et al., J. Sol-Gel Sci. Technol. **83** (2017) 394.
46. S Park et al., J. Mater. Sci. Mater. Electron. **24** (2013) 4906.
47. H Lu et al., J. Phys.: Condens. Matter **20** (2008) 472202.